

Nonlinear Unsteady Vortex-Lattice Vortex-Particle Method with Adaptive Wake Conversion for Rotorcraft Aerodynamics

Jinbin Fu^{*} and Eric Laurendeau[†]

Polytechnique Montréal, Montréal, Quebec, Canada, H3T 1J4

Nonlinear unsteady vortex lattice–vortex particle methods (NL-UVLM-VPM) provide medium-fidelity predictions of rotorcraft aerodynamics with explicit three-dimensional wake representations at a moderate computational cost. This study presents an NL-UVLM-VPM approach with a scale-consistent adaptive wake panel-particle conversion strategy that mitigates the inherent temporal–spatial resolution coupling of conventional wake treatments in rotorcraft aerodynamic simulations. Numerical assessment shows that this strategy preserves the near third-order temporal convergence of the underlying time-integration scheme while improving robustness under coarsened temporal resolution. For a representative hover case, computational time is reduced by 29% relative to the conventional conversion strategy at identical temporal resolution and by nearly 70% compared with a fine-resolution reference simulation over 20 rotor revolutions, while maintaining thrust and torque predictions within 1% of the reference solution. Based on these analyzes, practical recommendations for particle conversion parameters and wake resolution are provided. The methodology is further validated for increasingly complex scenarios, including hover, forward flight with blade–vortex interaction, and multirotor interaction. Predictions show good agreement with experimental data and dedicated unsteady Reynolds-averaged Navier–Stokes simulations (URANS), while computational speedups exceeding two orders of magnitude relative to URANS are achieved.

Nomenclature

C_D	=	airfoil drag coefficient, $D/(1/2)\rho_\infty U_\infty^2 c$
C_L	=	airfoil lift coefficient, $L/(1/2)\rho_\infty U_\infty^2 c$
C_P	=	sectional pressure coefficient, $P/(1/2)\rho_\infty U_\infty^2$
C_Q	=	torque coefficient, $Q/\rho_\infty U^2 \pi R^3$
C_T	=	thrust coefficient, $T/\rho_\infty U^2 \pi R^2$
c	=	chord length, m

^{*}Post-doctoral fellow, Department of Mechanical Engineering, Polytechnique Montréal, jinbin.fu@polymtl.ca, jinbin.fu@polimi.it

[†]Professor, Department of Mechanical Engineering, Polytechnique Montréal, eric.laurendeau@polymtl.ca, AIAA Senior Member

c_V	=	the standard Vreman subgrid-scale model coefficient
$d\mathbf{l}$	=	vector length of the straight-line vortex segment, m
M	=	Mach number
N_{rev}	=	number of rotor revolutions
N_b	=	number of blades per rotor
N_p	=	number of vortex particles
N_{steps}	=	number of time steps per rotor revolution
n_c	=	number of panel chordwise discretization
n_i	=	number of particles assigned at the i -th straight-line element
n_s	=	number of panel spanwise discretization
n_t	=	number of particles assigned at the tip vortex segment
Q	=	rotor torque, $N \cdot m$
R	=	rotor radius, m
R_c	=	cut-out rotor radius, m
Re	=	Reynolds number
r	=	radius position, m
T	=	rotor thrust, N
t	=	time, s
u	=	velocity, m/s
\mathbf{x}_i	=	the position of the i -th particle, $\mathbf{x}_i(t)$, m
α	=	angle of attack, deg
ψ	=	azimuthal angle, deg
θ	=	blade pitch angle, deg
β	=	blade flap angle, deg
δ	=	blade lead-lag angle, deg
Γ_i	=	vortex strength of i th particle, $\Gamma_i(t)$, m^3/s
ρ	=	3D Gaussian smoothing function parameter
ρ_∞	=	air density, kg/m^3
σ	=	filter width (smoothing radius or core size), m
ζ_σ	=	3D Gaussian distribution, $1/m^2$
ν	=	kinematic viscosity, m^2/s
ω	=	vorticity field, $\omega(\mathbf{x}, t)$, $1/s$

Δx_{tip} = blade tip particle spacing, deg
 $\Delta \Psi$ = blade azimuthal increment, deg

Subscripts

extrap = Richardson extrapolation

I. Introduction

MODELING rotorcraft aerodynamics accurately and efficiently remain significant challenges due to the highly complex aerodynamic environment inherent to rotor systems. With the increasing interest in urban air mobility (UAM), there is a growing demand for aerodynamic tools that balance fidelity and computational cost. High-fidelity approaches such as three-dimensional(3D) unsteady Reynolds-Averaged Navier-Stokes (URANS) and Scale-Resolving Simulations (SRS) can capture detailed flow physics but require fine spatial resolution to mitigate numerical dissipation and remain computationally expensive for long-duration simulations.[1–4].

To reduce computational cost while retaining essential wake physics, several classes of mid-fidelity aerodynamic tools for rotor analysis have been developed. Hybrid approaches combining potential-flow blade models with free-wake or vortex particle methods (VPM) are widely used [5–11]. Representative implementations include the DLR unsteady panel method (UPM) [5] and DUST software [10]. In parallel, particle-based rotor formulations employing actuator-line or actuator-surface representations have also been explored, as exemplified by FlowUnsteady [12]. Collectively, these methods enable rotor performance prediction at substantially lower computational costs than high-fidelity grid-based CFD while preserving dominant wake structures.

Within this context, the authors’ research group developed a hybrid nonlinear unsteady vortex lattice-vortex particle method (NL-UVLM-VPM) incorporating a viscous-inviscid α -coupling strategy supported by a two-dimensional (2D) RANS database and a Particle Strength Exchange (PSE)-based viscous diffusion model within a Large Eddy Simulation (LES) framework. As reported in Ref. [13], the method achieved good correlation with experimental data for the hover performance of the S-76 rotor model. However, that validation was limited to steady performance prediction, and the predictive capability of the approach in more complex unsteady aerodynamic environments, such as forward flight and multirotor interaction, remains insufficiently validated. These operating conditions introduce additional challenges, including wake skewing, blade-vortex interaction, and rotor-rotor interaction, which require further systematic assessment.

In conventional hybrid UVLM-VPM implementations, wake particles are shed at every time step, inherently coupling temporal and spatial discretizations, which introduces a trade-off between computational efficiency, spatial resolution, and numerical robustness [11]. Relaxing temporal resolution to improve efficiency reduces wake resolution and degrades predictive accuracy, whereas increasing particle density to maintain spatial resolution can compromise numerical

robustness. As a result, this spatio-temporal coupling limits the resolution flexibility and numerical robustness of long-duration simulations.

Building upon the current NL-UVLM-VPM solver, the present work introduces a scale-consistent adaptive wake panel-particle conversion strategy based on the geometric streamwise length of trailing vortex segments. By assigning particle density proportional to the actual wake-segment arc length, this method improves resolution consistency along the rotor wake, thereby mitigating the inherent temporal-spatial discretization trade-off.

The objectives of this study are threefold. First, to introduce an adaptive wake panel-particle conversion strategy within the NL-UVLM-VPM framework. Second, to assess its numerical convergence, robustness, and algorithmic efficiency in representative hover simulations, and to provide practical recommendations for numerical stability and efficiency. Third, to extend the validation envelope of the solver beyond hover and evaluate its predictive capability and computational cost under more complex operating conditions, including forward flight and rotor-rotor interaction, through comparisons with dedicated URANS simulations and available experimental data.

The remainder of this paper is organized as follows. Section II summarizes the NL-UVLM and VPM formulations and presents the adaptive wake panel-to-particle conversion strategy. Section III examines the numerical convergence, robustness, and algorithmic efficiency of the adaptive conversion method, including a temporal-resolution sensitivity study and recommended parameter settings. Section IV provides validation results for benchmark rotor configurations, including hover, forward flight, and rotor-rotor interaction cases, with comparisons against URANS simulations and experimental measurements, together with an assessment of overall computational cost. Finally, the main conclusions are summarized in Section V.

II. Numerical Methods

A. Nonlinear unsteady vortex-lattice method (NL-UVLM)

The unsteady vortex-lattice method (UVLM) is a low-order computational technique for solving unsteady potential flow around lifting surfaces. A detailed description of this method can be found in Ref. [13]. Here, a summary is presented for completeness and to help understand the additional developments presented later in the paper.

As shown in Fig. 1, in rotor simulations, the blade geometry is treated as a thin body composed of lifting surfaces, and the wake is represented as a set of vortex panels. The blade and wake are simulated using the classical vortex-lattice method [14] with time-stepping, referred to as the unsteady vortex-lattice method (UVLM). Specifically, the blade planform is simplified to a flat surface between the leading and trailing edges, discretized using a structured grid. Vortex ring elements are placed at the quarter-chord location of each grid element. For the wake, vortex panels extend from the trailing edge to infinity, with the Kutta condition applied to ensure that the circulation equals zero.

The induced velocity from each vortex ring element is computed using the Biot-Savart law, with the Vatis

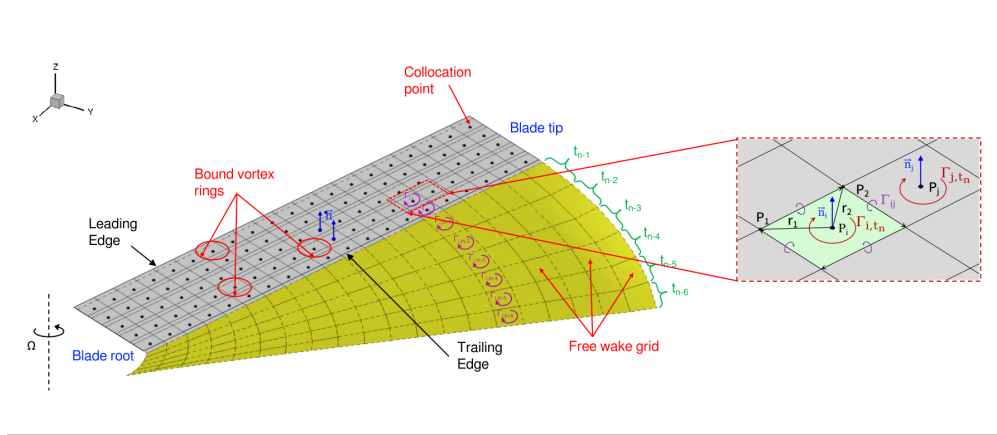


Fig. 1 Descriptive diagram of the Unsteady Vortex-Lattice Method (UVLM).

smoothing kernel [15] to eliminate the singularity in the Biot-Savart equation during wake displacement in the rotor simulations. A Neumann boundary condition, which enforces the local velocity to be tangent to the vortex ring element, is applied to the collocation points. These points are located at the center of the three-quarter-chord line of each lifting surface panel. This treatment ensures that the vortex rings generate lift with a slope consistent with thin airfoil theory.

To include nonlinear effects, a low computational cost viscous-inviscid α -iterative coupling algorithm is applied to each chordwise strip of vortex panels along the span of the blade. Each strip is corrected using a 2D viscous database formatted as a .c81 table, which has been calculated with CHAMPS [16]. The iterative viscous coupling is detailed in Proulx-Cabana's work [13].

Aerodynamic loads are determined by integrating the UVLM solution with the viscous section data, taking advantage of the availability of both information. The steady component of the loads is computed on each panel side from the Kutta-Joukowski theorem [17], while the unsteady component is evaluated at the center of every panel through the unsteady Bernoulli equation [17].

B. Vortex particle method (VPM)

The vortex particle method is a Lagrangian, grid-free approach that models the evolution of free wakes using viscous vortex particles to construct the vorticity field governed by the velocity-vorticity formulation of the incompressible Navier-Stokes equations:

$$\frac{D\boldsymbol{\omega}}{Dt} = (\boldsymbol{\omega} \cdot \nabla)\mathbf{u} + \nu\nabla^2\boldsymbol{\omega} \quad (1)$$

where $\boldsymbol{\omega} = \nabla \times \mathbf{u}$ is the vorticity field associated with the velocity field, and ν is the kinematic viscosity of the flow. The first term on the right-hand side of Eq. (1) is the vortex stretching term that controls the stretching and deformation of the vortex, while the second term represents the viscous diffusion effects.

In VPM, the vorticity field can be expressed in a Lagrangian manner as the sum of the contributions of a set of N_p

vector-valued particles, i_p :

$$\boldsymbol{\omega}(\mathbf{x}, t) = \sum_{i=1}^{N_p} \boldsymbol{\Gamma}_i(t) \zeta_\sigma(\mathbf{x} - \mathbf{x}_i(t)) \quad (2)$$

where $\mathbf{x}_i(t)$ and $\boldsymbol{\Gamma}_i(t)$ are the position and vorticity intensity, respectively, of the i -th particle. $\zeta_\sigma(\mathbf{x})$ is a smooth function, where σ is the smoothing radius that is greater than the distance between particles to guaranty the convergence of VPM [18]. In this work, the 3D Gaussian distribution is adopted as the smooth function:

$$\zeta_\sigma(\rho) = \frac{1}{(2\pi\sigma^2)^{3/2}} e^{-\rho^2/2} \quad \text{and} \quad \rho = \frac{|\mathbf{x} - \mathbf{x}_i(t)|}{\sigma} \quad (3)$$

the parameter σ is defined as the maximum distance from all neighboring particles in both the streamwise and spanwise directions, and it remains constant throughout the simulation.

Based on Eq. (1), the evolution of viscous vortex particles can be represented by the system of ordinary differential equations in convection-diffusion form,

$$\frac{d\mathbf{x}_i(t)}{dt} = \mathbf{u}_i(t) \quad (4)$$

$$\frac{d\boldsymbol{\Gamma}_i(t)}{dt} = (\boldsymbol{\Gamma}_i(t) \cdot \nabla^T) \mathbf{u}_i(t) + \nu \nabla^2 \boldsymbol{\Gamma}_i(t) \quad (5)$$

where $i = 1, \dots, N_p$ for all particles. The first equation, which describes the convection of the i -th vortex particle transported by the local flow velocity, is adopted to update the particle positions. The second equation expresses the effect of vortex stretching and diffusion on the vorticity intensity of the i -th vortex particle. In this work, both the particle positions and the vorticity intensity are advanced in time using the low-storage third-order Runge-Kutta scheme [19]. A Cartesian fast multipole method (FMM) is used to accelerate the calculation of the induced velocity and its gradient for vortex particles, reducing the numerical complexity from $O(N^2)$ to $O(N)$ [13].

The viscous diffusion term, which accounts for the effect of air viscosity on vorticity transportation, is solved using the PSE algorithm. To mitigate the instability of vortex stretching that may arise from insufficient viscous dissipation at subgrid scales – caused by the incomplete resolution of the full turbulent energy cascade described by Kolmogorov’s theory [20] – the Vreman subgrid scale (SGS) model [21] is adopted to compute turbulent eddy viscosity. This approach allows for modeling eddies at smaller scales and capturing coherent structures at coarser spatial resolutions than those required for direct numerical simulation (DNS). Further details can be found in a previous paper [13]. In the present work, the Vreman model coefficient C_V is set to 0.07, consistent with the value used in Ref. [13].

Fig. 2 presents a DJI Phantom II rotor wake from the current VPM simulation at an advance ratio of $J = 0.35$. The simulation is able to capture every stage of the wake, from a coherent vortex structure to turbulent breakdown and mixing, and it predicts transitional mechanisms in between, such as short-wave instability, leapfrog, and pairing.

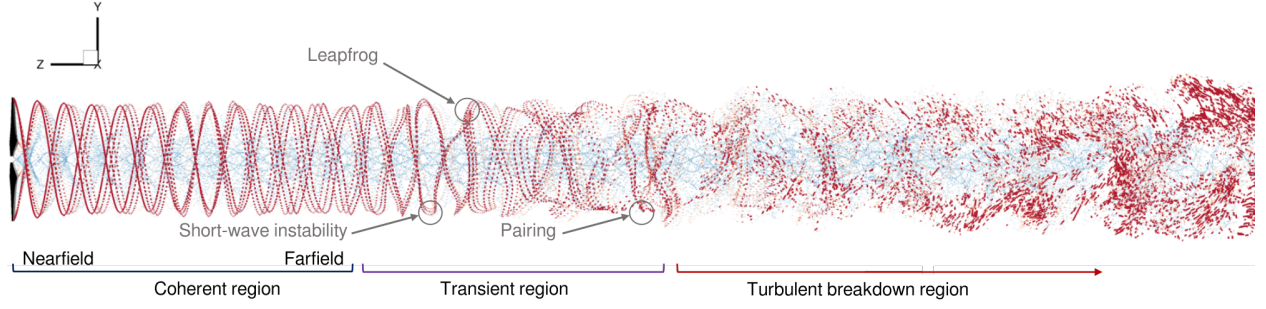


Fig. 2 The current VPM simulation capturing the wake evolution of a DJI Phantom II rotor at $J = 0.35$ from a coherent vortical structure to turbulent breakdown and mixing.

C. Adaptive wake panel-particle conversion strategy

In hybrid UVLM-VPM approaches, wake panels are commonly converted into vortex particles after a prescribed number of time steps to prevent excessive geometric distortion and numerical instability associated with panel stretching. Following this approach, the wake shed from the blade trailing edge is initially represented as straight-line vortex elements, with the strength of upstream vortex lines remaining unchanged to prevent circulation strength discontinuity at the trailing edge. These wake panels are then converted into vortex particles after a prescribed number of time steps, as illustrated in Fig. 3. Here, the streamwise particles (shown in green) represent trailed particles, and the spanwise particles (shown in red) are shed particles. The strength of each new particle is proportional to the circulation difference between two adjacent wake panels, as given by:

$$\Gamma_i = \frac{\Delta\Gamma_i d\mathbf{l}}{n_i} \quad (6)$$

where $d\mathbf{l}$ is the vector length of the straight-line vortex element, n_i is the number of particles approximating the i -th straight-line element, and $\Delta\Gamma_i$ represents the circulation difference between two wake panels on either side of the edge. It can be defined as:

$$\Delta\Gamma_i = \begin{cases} \Gamma_i - \Gamma_{i_n}, & \text{if neighbour } i_n \text{ present} \\ \Gamma_i, & \text{if neighbour } i_n \text{ absent} \end{cases} \quad (7)$$

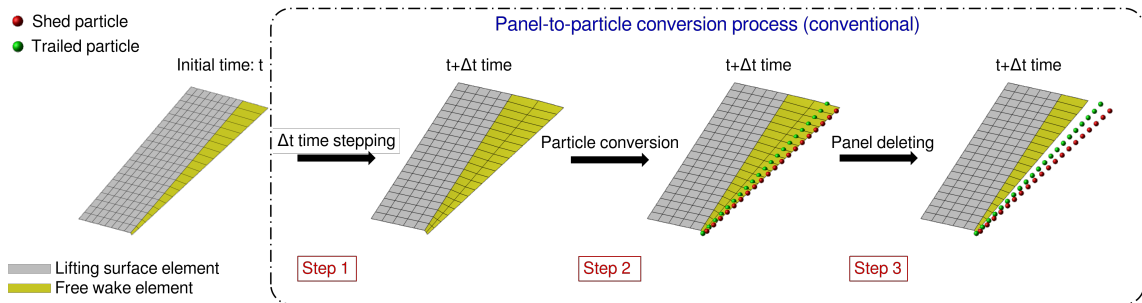


Fig. 3 The conventional conversion process of wake panels to particles ($n_i = 1$)

In the conventional wake panel-particle conversion strategy, each trailing vortex segment is discretized into an identical number of particles, regardless of its streamwise length. In rotor simulations, however, the streamwise length of trailing vortex segments increases with radial position, resulting in substantial variations in wake-segment geometry along the blade span. When uniform particle conversion is applied, this geometric inconsistency produces highly non-uniform spatial resolution, inefficient particle distribution, and degraded computational performance.

To improve resolution consistency, the present work introduces a scale-consistent adaptive wake panel-particle conversion strategy, in which the number of particles assigned to each trailing vortex segment is proportional to its actual streamwise arc length based on the prescribed particle count at the blade tip vortex segment. Let Δs_i denote the streamwise length of the i -th trailing vortex segment and Δs_t the reference length at the blade tip. Prescribing n_t particles for the tip segment, the number of particles assigned to segment i is defined as:

$$n_i = \left\lceil \frac{\Delta s_i}{\Delta s_t} \cdot n_t \right\rceil \quad (8)$$

where $\lceil \cdot \rceil$ denotes upward rounding. Fig. 4 illustrates the resulting particle distribution obtained using the adaptive conversion method ($n_t = 2$). For clarity, the shed particles are omitted to highlight the conversion procedure. It can be observed that this adaptive scaling significantly improves spatial resolution consistency along the wake.

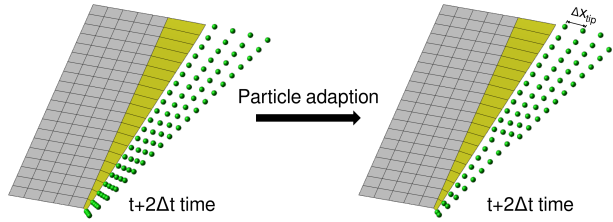


Fig. 4 The adaptive conversion process of wake panels to particles ($n_t = 2$) after two time steps.

III. Numerical Convergence, Robustness and Efficiency of the Adaptive Conversion Strategy

A. Resolution definition and decoupled parameterization

To systematically assess the influence of the adaptive wake panel-particle conversion strategy on the temporal-spatial discretization behavior of the NL-UVLM-VPM solver, independent parameters are introduced to control temporal and wake spatial resolution. The temporal resolution is defined by the number of time steps per revolution, N_{steps} , from which the blade azimuthal increment is obtained as

$$\Delta\Psi = \frac{360^\circ}{N_{\text{steps}}} \quad (9)$$

The wake spatial resolution is independently controlled through the prescribed tip particle spacing,

$$\Delta x_{\text{tip}} = \frac{\Delta \Psi}{n_t} \quad (10)$$

where n_t denotes the number of particles assigned to the blade-tip vortex segment. This parameterization enables variation in temporal resolution while maintaining constant wake spatial fidelity, therefore allowing direct assessment of the decoupling behavior introduced by the adaptive conversion strategy.

B. Convergence behavior

The convergence properties of the adaptive conversion strategy are evaluated using the Caradonna-Tung rotor in hover ($M_T = 0.439$, $\theta_c = 5^\circ$). Default parameters $N_{\text{steps}} = 144$, $\Delta x_{\text{tip}} = 2.5^\circ$, $n_s = 20$, and $n_c = 8$ are adopted as following the convergence studies reported in prior work [13], and serve as the reference case. In the present work, $\Delta \Psi$ is varied independently while maintaining the Δx_{tip} constant, so as to evaluate the convergence behavior of the adaptive conversion algorithm without the influence of wake spatial refinement, and the thrust coefficient, C_T , is employed as the convergence metric.

Fig. 5 shows the convergence properties of the thrust coefficient, C_T , as the temporal resolution is refined by increasing the number of time steps per revolution, N_{steps} , from 9 to 144, corresponding to blade azimuthal increments of 40° and 2.5° , respectively. Over this refinement range, the number of tip particles generated per revolution varies from $n_t = 16$ to $n_t = 1$. The corresponding Richardson extrapolation is also shown. An approximation of the convergence order, p , is obtained by fitting the numerical results to the model

$$C_T = (C_T)_{\text{extrap}} + a(\Delta t)^p, \quad (11)$$

where $\Delta t \propto 1/N_{\text{steps}}$, and the fitted curve is plotted as a solid line in the figure. The resulting convergence order is $p = 2.83$. This near third-order convergence confirms that the adaptive conversion strategy does not degrade the temporal accuracy of the third-order Runge-Kutta time integration used in the VPM solver. For $N_{\text{steps}} \geq 72$, the relative deviation in C_T remains below 1% with respect to the reference solution.

C. Numerical robustness under relaxed temporal resolution

Fig. 6 compares the long-term behavior of the conventional and adaptive conversion strategies for coarse temporal discretizations. For $N_{\text{steps}} = 18$ to 36, the conventional conversion exhibits numerical instability after approximately 8 and 10 rotor revolutions, manifested by divergence in C_T . In contrast, the adaptive conversion maintains stable solutions for 20 rotor revolutions across all tested temporal resolutions. The improved robustness is attributed to geometry-consistent scaling of particle density, which mitigates excessive near-root particle clustering and suppresses

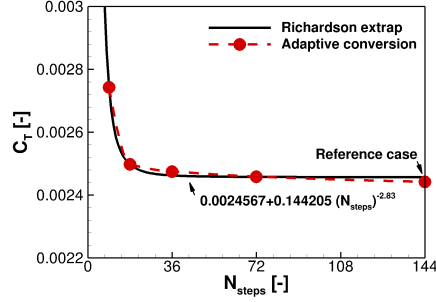


Fig. 5 The adaption conversion convergence study of the helicopter rotor simulation.

the growth of spurious numerical oscillations under relaxed temporal discretization. These results demonstrate that the adaptive strategy effectively alleviates the inherent temporal–spatial discretization trade-off present in the conventional conversion strategy.

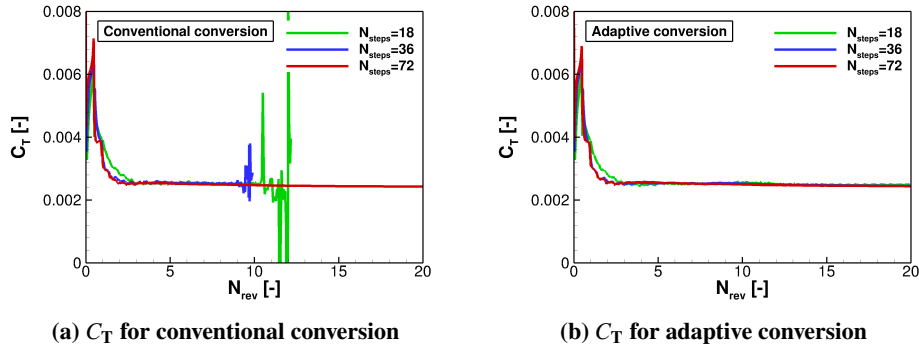


Fig. 6 Convergence comparison of wake panel-particle conversion strategies.

D. Algorithmic efficiency and practical recommendation

Table 1 provides quantitative comparisons of particle count and wall-clock time. All computations were conducted on a single AMD EPYC 9655 (Zen 5)@2.6 GHz processor with 96 cores and 192 threads for 20 rotor revolutions.

Table 1 Quantitative assessment of panel-particle conversion strategies.

Case	C_T deviation	C_Q deviation	Particles count	CPU wall-time
Reference ($N_{\text{steps}} = 144, n_t = 1$)	—	—	235996	8.0 h
Conventional ($N_{\text{steps}} = 72, n_t = 2$)	+0.7%	+0.09%	178312	3.5 h
Adaptive ($N_{\text{steps}} = 72, n_t = 2$)	+0.6%	+0.09%	146676	2.5 h

At identical temporal resolution ($N_{\text{steps}} = 72$), the adaptive strategy reduces particle count by approximately 18% and wall time by about 29% relative to the conventional conversion, while maintaining comparable deviations in C_T and C_Q . When compared with the fine-resolution reference case ($N_{\text{steps}} = 144$), the adaptive strategy enables an overall reduction of approximately 38% in particle count and nearly 70% in computational wall time, while preserving deviations in C_T

and C_Q within 1%.

Based on the present analysis, a temporal resolution corresponding to a 5° azimuthal increment ($N_{\text{steps}} = 72$) combined with $\Delta x_{\text{tip}} = 2.5^\circ$ provides an effective balance between temporal accuracy, numerical robustness, and computational efficiency. Unless otherwise specified, this configuration is adopted for all subsequent validation cases.

IV. Case validation

Following the numerical convergence, robustness, and efficiency assessment presented in Sec. III, this section evaluates the predictive capability of the NL-UVLM-VPM solver with the adaptive conversion strategy under progressively more complex aerodynamic conditions. In contrast to previous studies [13] in which validation was limited to hover conditions, the present assessment extends the validation envelope to forward flight and multi-rotor interaction scenarios.

Three benchmark rotor cases are considered. The first case, described in Sec. IV.A, considers the two-bladed Caradonna-Tung rotor in hover [22], serving as a baseline evaluation of steady performance and near wake predictions. The second case, presented in Sec. IV.B, investigates the full-scale AH-1G main rotor in forward flight [23], characterized by pronounced unsteady loading and BVI phenomena. Finally, Sec. IV.C studies a side-by-side rotor configuration [24] to assess the solver’s ability to capture rotor-rotor aerodynamic interference and induced flow interaction effects. Collectively, these cases examine the method’s robustness and predictive consistency across increasing levels of aerodynamic complexity.

A. Hovering case: Caradonna-Tung rotor

The Caradonna and Tung (C-T) hovering rotor case [22] is selected as a baseline validation configuration. The two-bladed rotor features untwisted rectangular blades with a NACA0012 airfoil and an aspect ratio of 6. The test conditions considered in this study are reported in Table. 2.

Table 2 Hover test conditions for C-T rotor[22]

Collective pitch (θ_c)	Blade Tip Mach number (M_T)
5°	
8°	0.439
12°	

High-fidelity URANS simulations are performed using the ROSITA solver [25] on a Chimera grid system containing 8.65 million cells. A medium resolution grid, previously verified through grid-convergence studies, is adopted. Due to the time-accurate formulation, each revolution requires approximately 16 hours on 240 processors. In NL-UVLM-VPM simulations, a total of 20 rotor revolutions are computed to allow sufficient wake development and periodic convergence of the aerodynamic loads.

Fig. 7 compares the predicted integrated thrust coefficient C_T with experimental measurements and URANS results

for three collective pitch angles. The NL-UVLM-VPM predictions show close agreement with experimental data across all loading conditions and exhibit smaller deviations than the URANS results.

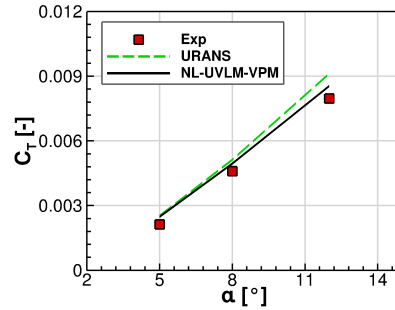


Fig. 7 Comparison of integrated rotor thrust coefficient on various collective pitch angles.

The chordwise pressure coefficient (C_p) distributions at radial positions of $r/R = 0.68, 0.80,$ and 0.89 for $\theta_c = 5^\circ$ are presented in Fig. 8. In the NL-UVLM-VPM solution, pressure coefficients are reconstructed from the 2D RANS database using the effective angle of attack at each blade section. It can be seen that the predicted pressure distributions agree well with both experimental and URANS data for all radial positions. However, minor discrepancies become more significant toward the blade tip, primarily due to three-dimensional effects and strong tip-vortex influence.

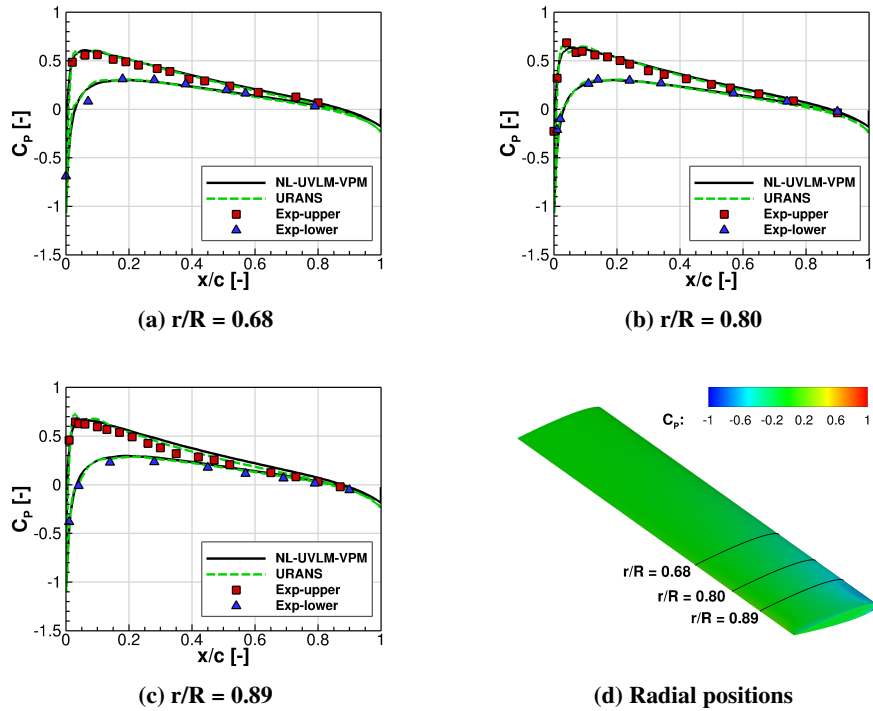


Fig. 8 C_p distribution over blade chord in different radial position for C-T rotor blade at $\theta_c = 5^\circ$.

Fig. 9 compares the predicted tip vortex trajectories with experimental measurements and URANS results at three

collective pitch settings. The NL-UVLM-VPM method captures the radial contraction and axial convection trends of the tip vortex across all loading conditions. At higher collective pitch, both numerical approaches present increasing deviation from experimental trajectories, reflecting the sensitivity of wake geometry to induced velocity modeling at higher thrust levels. Nevertheless, the overall contraction and descent trends remain in good agreement. These results indicate that the NL-UVLM-VPM solver with the adaptive conversion strategy reliably resolves rotor performance and near-wake geometry in hover flight.

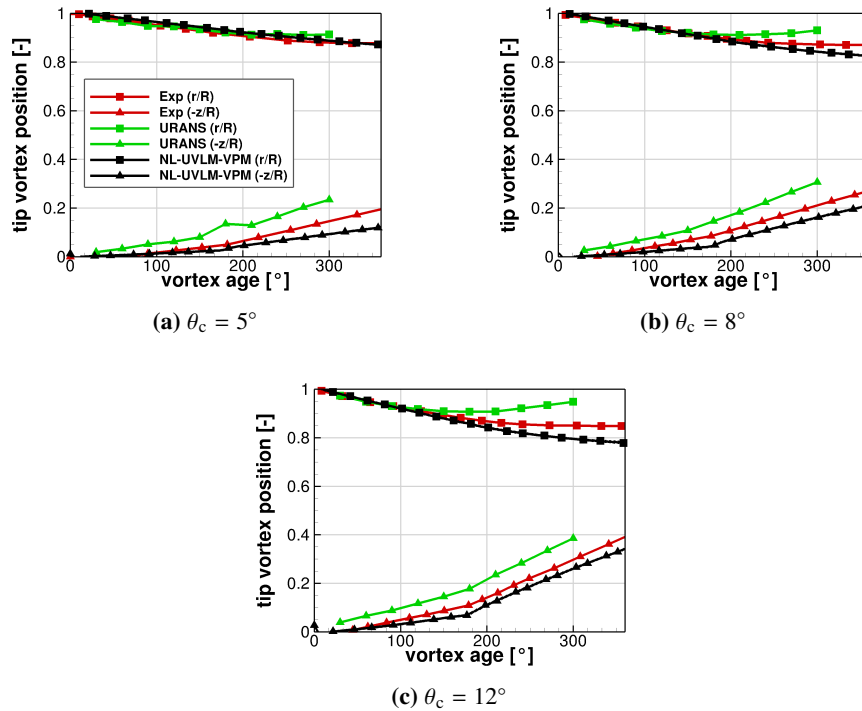


Fig. 9 Tip vortex position of C-T rotor for different collective pitch θ_c .

B. Forward flight case: AH-1G main rotor

This section evaluates the predictive capability of the mid-fidelity framework under forward flight conditions. The AH-1G main rotor test case [23] is considered as a representative configuration featuring pronounced unsteady aerodynamic loading and BVI phenomena.

The rotor geometry is summarized in Table. 3. The blade pitch and flapping motions are prescribed by the flight test measurements, as given in Eq. (12). The low-speed operating condition corresponds to test point 2157, with an advance ratio of 0.19 and a blade tip Mach number of 0.65.

$$\begin{aligned}\theta(\psi) &= 6.0 + 1.7 \cos(\psi) - 5.5 \sin(\psi) \\ \beta(\psi) &= 2.13 \cos(\psi) - 0.15 \sin(\psi)\end{aligned}\tag{12}$$

Table 3 Geometric properties [23]

Rotor property	Given value
N_b	2
Blade planform	Rectangular
Blade section	OLS/TAAT
R	6.7 m
c	0.7283 m
θ_{tw}	Linear, -10.0°
R_c	0.154R

High-fidelity URANS solutions are obtained using the ROSITA URANS solver [1] on a Chimera grid system comprising 11.1 million cells. Each revolution requires approximately 10 hours on 360 cores. In the mid-fidelity analysis, the 2D viscous database was obtained from the CHAMPS solver [16], covering an appropriate range of Reynolds numbers, Mach numbers, and angles of attack.

Fig. 10 presents the time history of the integrated thrust coefficient over ten revolutions. After approximately two revolutions, both URANS and NL-UVLM-VPM solutions reach a quasi-periodic state with nearly identical amplitudes and phase variations. The two predictions remain closely overlapped throughout subsequent revolutions, indicating that the present mid-fidelity method accurately reproduces the unsteady thrust response observed in the URANS simulation under forward-flight conditions.

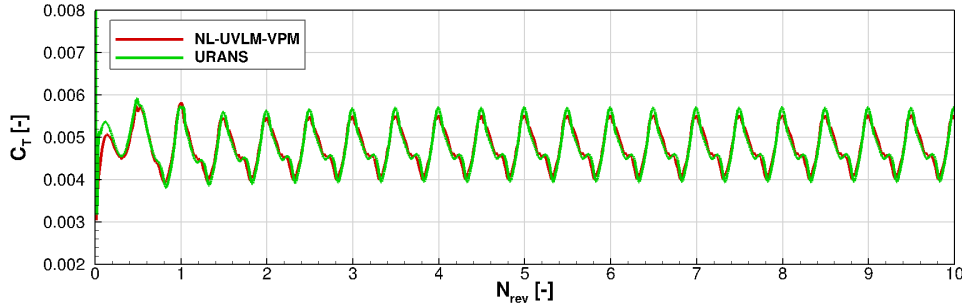


Fig. 10 Time history of the integrated thrust coefficient C_T over 10 rotor revolutions for the AH-1G rotor in forward flight.

For comparison with the flight test measurements, the thrust coefficients were smoothed using a simple moving average (SMA) method. This post-processing procedure eliminates oscillations and enables a direct comparison of the average aerodynamic trends across three datasets. As summarized in Table. 4, both numerical results slightly overpredict the experimental value, with deviations below 3%. The NL-UVLM-VPM prediction closely correlated with the URANS result, confirming its reliability for overall thrust performance prediction in forward flight.

To assess the accuracy of the mid-fidelity simulation at a local level, Fig. 11 shows the chordwise pressure coefficient distributions at several azimuthal positions ($\psi = 75^\circ, 90^\circ, 105^\circ, 270^\circ, 285^\circ, \text{ and } 300^\circ$) for the specific radial station

Table 4 Integrated thrust coefficient comparisons

Method	C_T	Errors
Experiment[23]	0.00464	-
URANS	0.00476	2.6%
NL-UVLM-VPM	0.00478	3.0%

($r/R = 0.91$). Overall, the NL-UVLM-VPM predictions agree well with both flight measurements and URANS results across the advancing and retreating sides. On the advancing side, both numerical methods capture the suction peak near the leading edge, which is associated with the high dynamic pressure as the advancing blade experiences increased relative inflow velocity. On the retreating side, a strong suction spike is observed experimentally, which is reproduced more clearly by URANS, while the NL-UVLM-VPM solution shows a slightly attenuated peak. Nevertheless, both approaches follow the overall pressure recovery trend.

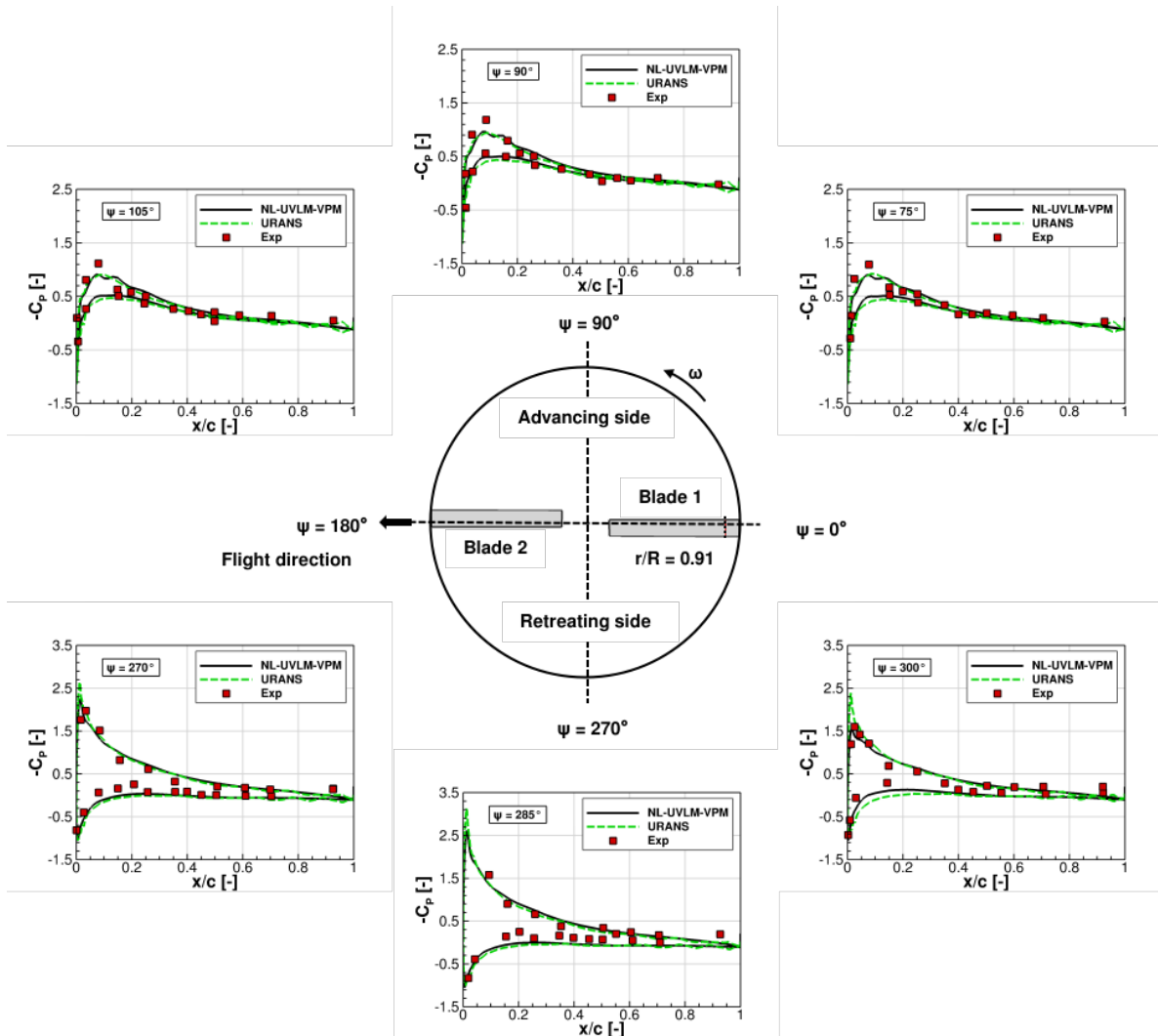


Fig. 11 Pressure coefficient distribution at $r/R = 0.91$ for AH-1G main rotor in forward flight.

Fig. 12 illustrates the sectional thrust coefficient variation at $r/R = 0.75$ and 0.91 over one rotor revolution. The NL-UVLM-VPM predictions show good agreement with both the flight test measurements and URANS simulations in terms of magnitude and phase across most azimuthal angles. Both numerical approaches overpredict the thrust on the advancing (0° to 90°) and retreating (300° to 360°) sides. These discrepancies are likely related to the absence of aeroelastic effects on the rotor blades in the present simulations, which can alter the effective angle of attack and the phase of the blade loads during flight. BVI signatures are observed near azimuthal angles of approximately 60° to 120° and around 300° . The NL-UVLM-VPM solution captures these fluctuations, although their amplitude is somewhat underpredicted. The URANS results show smoother behavior in these regions, consistent with the numerical dissipation inherent to grid-based methods.

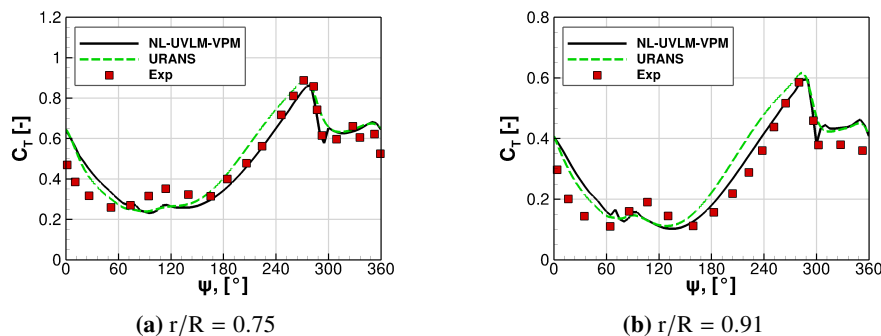


Fig. 12 Blade sectional thrust coefficients history over one rotor revolution.

The global wake topology is illustrated in Fig. 13, where vortex particles are colored by turbulent viscosity ν_t . It can be seen that the roll-up of the tip vortices on both the advancing and retreating sides, as well as their downstream convection, is clearly reproduced. The wake deformation in the forward flight region and the interaction between successive blade-tip vortices are also captured, demonstrating that the Lagrangian wake treatment maintains coherent vortex structures in forward flight.

C. Rotor-rotor interaction case: Large-scale side-by-side rotor

Building upon the single-rotor validations, this section assesses the mid-fidelity approach for multi-rotor aerodynamic interaction. Experimental data from Sweet's side-by-side rotor test in hover [24] are used for validation. The configuration consists of two identical counter-rotating rotors with an overlap ratio $L/R = 2.03$ and a phase difference of 90° , as shown in Fig. 14. The present study focuses on the high-solidity rotor configuration. The geometric and operating parameters are summarized in Table. 5.

High-fidelity reference solutions are obtained using time-accurate URANS simulations on a Chimera grid system comprising approximately 17.3 million cells. Each simulation requires three days to complete five rotor revolutions on 640 cores. Mid-fidelity simulations are performed for both an isolated single-rotor baseline and the side-by-side

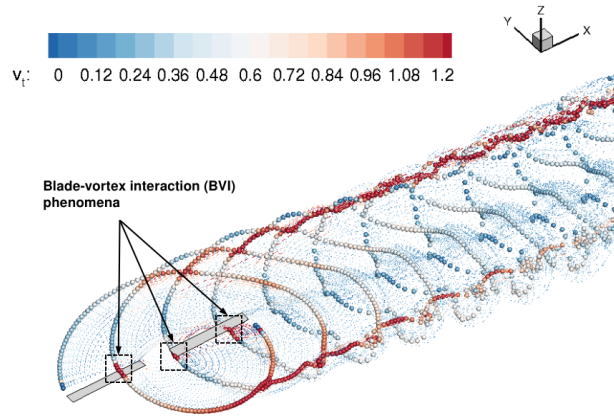


Fig. 13 Wake structures of AH-1G main rotor in forward flight.

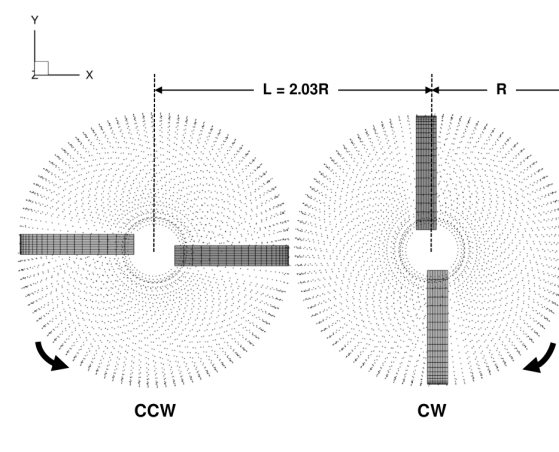


Fig. 14 Side-by-side rotor configuration, $L/R = 2.03$.

Table 5 Geometric properties and operating parameters[24]

Rotor property	Left rotor	Right rotor
N_b	2	2
Blade planform	Rectangular	Rectangular
Blade section	NACA0012	NACA0012
R	15.25 feet	15.25 feet
c	1.16 feet	1.16 feet
θ_{tw}	0°	0°
R_c	0.151R	0.151R
Rotational speed	626.18 RPM	-626.18 RPM

configuration. Hover conditions with varying collective pitch are considered to evaluate performance across different loading levels.

Fig. 15 compares the thrust-torque relationship and the figure of merit (FM) for the side-by-side configuration. The NL-UVLM-VPM predictions show good agreement with both experimental measurements and URANS results

across the tested thrust range. At high loading conditions (large C_T), where URANS data are available, both numerical approaches slightly underpredict FM relative to the experiment. This discrepancy may stem from the absence of aeroelastic deformation in the present simulations, which can affect rotor performance under elevated thrust levels.

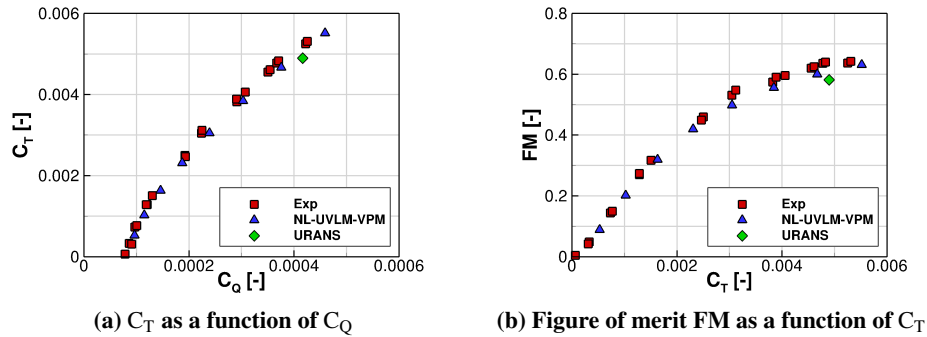


Fig. 15 Comparison of rotor performance for the side-by-side rotor model ($L/R = 2.03$).

Fig. 16 presents the spanwise distribution of the normal force coefficient (C_N) at three azimuthal phases for $\theta_c = 8^\circ$, with the single-rotor solution used as a reference. These results provide insight into the unsteady evolution of blade loading as the rotor interacts with the skewed wake and upwash field induced by the adjacent rotor. On the advancing side ($0^\circ \leq \psi \leq 90^\circ$), blade loading gradually recovers as the blade leaves the interaction region. During the transition phase ($90^\circ \leq \psi \leq 270^\circ$), the loading remains close to the single-rotor reference. Upon re-entry into the interference region on the retreating side ($270^\circ \leq \psi \leq 360^\circ$), noticeable inboard loading increase and outboard loading reduction are observed, reflecting the asymmetric induced flow field generated by rotor mutual interaction.

The colormaps of the instantaneous axial velocity fields at $N_{rev} = 10$, together with the velocity profiles extracted at $z/R = -0.5$ and $z/R = -1.0$, are displayed in Fig. 17, where the URANS results are included for comparison. The contours clearly capture two dominant downwash regions beneath the rotors and a weaker interaction region between them. As the wake convects downstream, the induced velocity cores move inward and partially merge, indicating wake contraction and mutual induction. This interaction produces a mildly asymmetric velocity distribution with localized upwash in the midplane, as reflected in the extracted velocity profiles. Meanwhile, the quantitative comparison of velocity profiles indicates a consistent representation of the dominant interaction-induced flow features between NL-UVLM-VPM and URANS.

Fig. 18 shows the instantaneous vortical structures identified using the Q-criterion ($Q = 0.005$) for both approaches. It can be seen that both simulations reproduce similar coherent helical tip vortices that roll up and convect downstream. A distinct inward contraction of the wake is observed, confirming the presence of mutual rotor induction. The NL-UVLM-VPM solution preserves dominant wake behavior, including tip-vortex roll-up, rotor mutual interaction, and wake skewness, in a manner consistent with those predicted by the URANS simulation. These alignments demonstrate

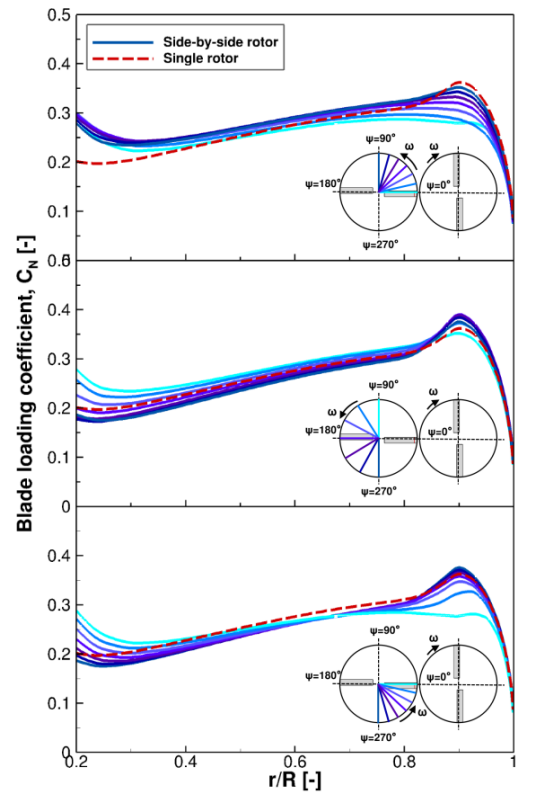


Fig. 16 Blade loading as blade goes through region of wake skewness and accentuated upwash between the rotors.

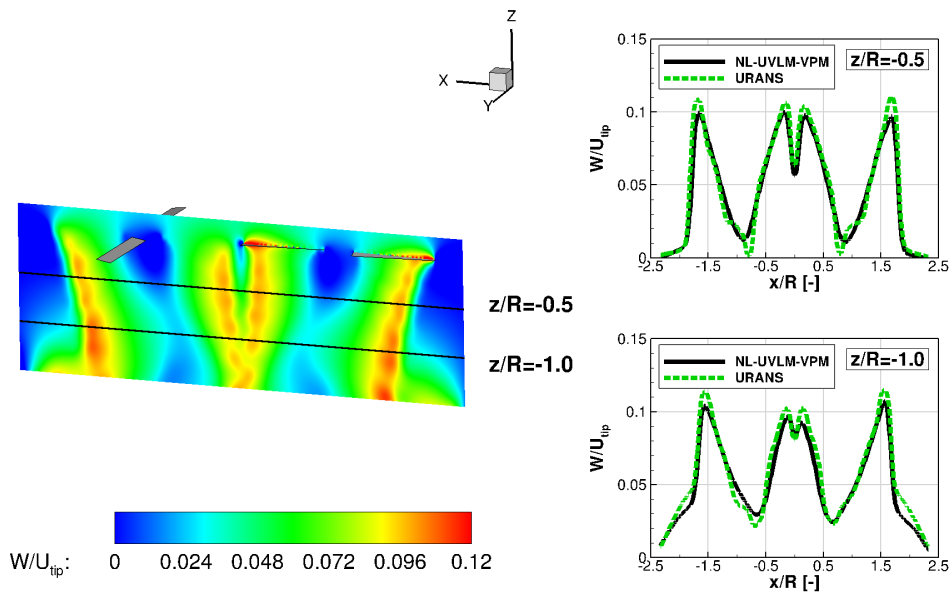


Fig. 17 Contour of the instantaneous velocity along the z-axis and velocity profiles extracted at $z/R = -0.5$ and -1.0 .

that the NL-UVLM-VPM approach effectively captures the essential physics of multi-rotor aerodynamic interaction.

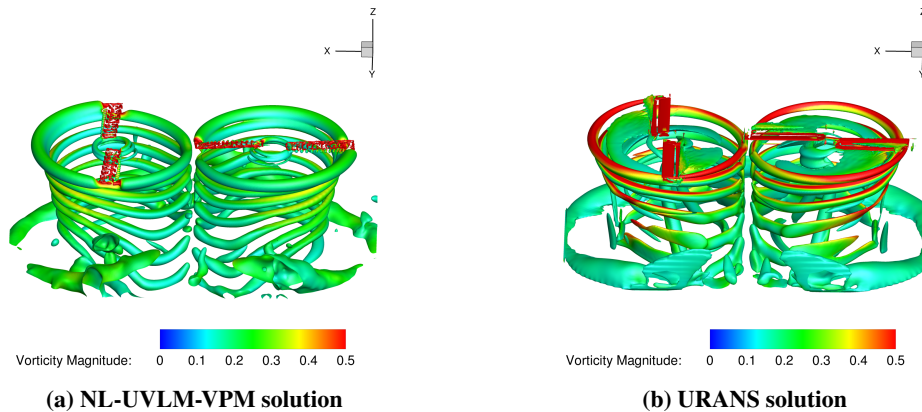


Fig. 18 Comparison between vortical structures obtained from NL-UVLM-VPM and URANS calculations.

D. Computational time

To assess computational efficiency, the average CPU time per revolution for the NL-UVLM-VPM and URANS simulations across all three benchmark cases is summarized in Table. 6. All computations were performed on the Niagara high-performance cluster at Compute Canada, which consists of 2024 nodes, each equipped with 40 Intel "Skylake" cores at 2.4 GHz, interconnected via an EDR Infiniband network.

The NL-UVLM-VPM approach requires significantly fewer computational resources than the corresponding time-accurate URANS simulations. Depending on the test case, the mid-fidelity solver achieves a speedup ratio exceeding two orders of magnitude. These results highlight the substantial reduction in computational cost offered by the mid-fidelity approach, while maintaining comparable predictions of aerodynamic loads and near-wake flow structures.

Table 6 CPU run-time of two approaches for all three test cases simulations

Test case	Approach	CPU cores	CPUh/rev	Speedup
C-T rotor	NL-UVLM-VPM	40	26	147.2
	URANS	240	3827	1.0
AH-1G rotor	NL-UVLM-VPM	40	25	142.4
	URANS	360	3560	1.0
Side-by-side rotor	NL-UVLM-VPM	40	53	173.9
	URANS	640	9216	1.0

V. Conclusions

The present study introduces a hybrid nonlinear unsteady vortex-lattice vortex-particle method with a scale-consistent adaptive wake panel-particle conversion strategy for rotorcraft aerodynamic simulations. The proposed strategy alleviates the inherent temporal–spatial resolution coupling of conventional wake treatments, enabling flexible control of wake

spatial resolution while preserving the temporal accuracy of the underlying time-integration scheme. Numerical assessments showed that the adaptive conversion strategy maintains near third-order temporal convergence and improves numerical robustness under coarsened temporal resolution.

For representative hover simulations, this approach reduced computational wall-clock time by approximately 29% relative to the conventional conversion strategy at identical temporal resolution, and by nearly 70% compared with a fine-resolution reference simulation over 20 rotor revolutions, while maintaining thrust and torque predictions within 1% of the reference solution. The study further provides practical recommendations for particle conversion parameters and wake resolution for numerical stability and computational efficiency.

The methodology was validated across a broadened range of operating conditions, including hover, forward flight with pronounced blade-vortex interaction, and side-by-side rotor aerodynamic interference. In these cases, good agreement with experimental measurements and dedicated high-fidelity URANS simulations was observed in integrated loads, sectional distributions, and dominant wake structures. In terms of computational cost, the present NL-UVLM-VPM framework achieves speedups exceeding two orders of magnitude in CPU-hours per revolution relative to time-accurate URANS for the cases considered, demonstrating the capability of this approach for accurate and efficient simulation of complex rotorcraft aerodynamic environments.

Future work will focus on extending the present method for complex tip geometries using the 2.5D hypothesis [26], incorporating rotor-fuselage interaction through panel method coupling, and integrating multidisciplinary effects such as aeroelasticity and aero-icing within the stripwise α -coupling approach.

Acknowledgments

The authors would like to thank Baptiste Arnould for his assistance with the CHAMPS Solver. This work was supported by the Natural Sciences and Engineering Research Council of Canada (NSERC), the Consortium de recherche et d'innovation en aérospatiale au Québec (CRIAQ), and CAE Inc. under the NSERC Alliance Grant (No. ALLRP 572207-22) and the CRIAQ project HAMAC. Calculations were performed on the Digital Research Alliance of Canada and Calcul Québec clusters. Lastly, we acknowledge the use of ChatGPT (GPT-5.2, 2026) for language polishing and editing.

References

- [1] Fu, J., and Vigevano, L., "An Efficient Helicopter Main Rotor Trim Method Based on Computational Fluid Dynamics," *49th European Rotorcraft Forum*, Bückeburg, Germany, 2023.
- [2] Chaderjian, N. M., and Ahmad, J. U., "Detached Eddy Simulation of the UH-60 Rotor Wake using Adaptive Mesh Refinement," *American Helicopter Society 68th Annual Forum*, Fort Worth, USA, 2012.

- [3] Narducci, R., “Hover Performance Assessment of Several Tip Shapes Using OVERFLOW,” *53rd AIAA Aerospace Sciences Meeting*, AIAA, Kissimmee, USA, 2015.
- [4] Jain, R., “Hover Predictions for the S-76 Rotor with Tip Shape Variation Using CREATE-AV Helios,” *53rd AIAA Aerospace Sciences Meeting*, AIAA, Kissimmee, USA, 2015.
- [5] Yin, J., and Ahmed, S., “Helicopter Main-Rotor/Tail-Rotor Interaction,” *Journal of the American helicopter society*, Vol. 45, 2000. <https://doi.org/10.4050/JAHS.45.293>.
- [6] Opoku, D. G., Triantos, D. G., Nitzsche, F., and Voutsinas, S. G., “Rotorcraft Aerodynamic and Aeroacoustic Modelling using Vortex Particle Methods,” *23rd International Congress of Aeronautical Sciences (ICAS 2002)*, Toronto, Canada, 2002.
- [7] Zhao, J., and He, C., “A Viscous Vortex Particle Model for Rotor Wake and Interference Analysis,” *Journal of the American Helicopter Society*, Vol. 50, No. 1, 2010. <https://doi.org/10.4050/JAHS.55.012007>.
- [8] Tan, J., and Wang, H., “Simulating Unsteady Aerodynamics of Helicopter Rotor with Panel/Viscous Vortex Particle Method,” *Aerospace Science and Technology*, Vol. 30, No. 1, 2013, pp. 255–268. <https://doi.org/10.1016/j.ast.2013.08.010>.
- [9] Lee, H., and Lee, D. J., “Numerical Investigation of the Aerodynamics and Wake Structures of Horizontal Axis Wind Turbines by Using Nonlinear Vortex Lattice Method,” *Renewable Energy*, Vol. 132, 2019, pp. 1121–1133. <https://doi.org/10.1016/j.renene.2018.08.087>.
- [10] Tugnoli, M., Montagnani, D., Syal, M., Droandi, G., and Zanotti, A., “Mid-fidelity Approach to Aerodynamic Simulations of Unconventional VTOL Aircraft Configurations,” *Aerospace Science and Technology*, Vol. 115, 2021. <https://doi.org/10.1016/j.ast.2021.106804>.
- [11] Yurt, M. K., Bolgul, B., and Yavrucuk, I., “Meshless Large Eddy Simulation of Rotorcraft Using GPUs,” *Vertical Flight Society’s 81st Annual Forum & Technology Display*, Beach, USA, 2025.
- [12] Alvarez, E. J., and Ning, A., “Stable Vortex Particle Method Formulation for Meshless Large-Eddy Simulation,” *AIAA Journal*, Vol. 62, No. 2, 2024, pp. 637–656. <https://doi.org/10.2514/1.J063045>.
- [13] Proulx-Cabana, V., Nguyen, M. T., Prothin, S., Michon, G., and Laurendeau, E., “A Hybrid Non-Linear Unsteady Vortex Lattice-Vortex Particle Method for Rotor Blades Aerodynamic Simulations,” *Fluids*, Vol. 7, No. 2, 2022. <https://doi.org/10.3390/aerospace7070090>.
- [14] Katz, J., and Plotkin, A., *Low-Speed Aerodynamics*, 2nd ed., Cambridge University Press, Cambridge, 2001.
- [15] Vatisstas, G. H., Kozel, V., and Mih, W. C., “A Simpler Model for Concentrated Vortices,” *Experiments in Fluids*, Vol. 11, No. 1, 1991, pp. 73–76. <https://doi.org/10.1007/BF00198434>.
- [16] Parenteau, M., Bourgault-Cote, S., Plante, F., and Laurendeau, E., “Development of Parallel CFD Applications on Distributed Memory with Chapel,” *34th IEEE International Parallel and Distributed Processing Symposium Workshops (IPDPSW 2020)*, New Orleans, USA, 2020.

- [17] Simpson, R. J., Palacios, R., and Murua, J., “Induced-Drag Calculations in the Unsteady Vortex Lattice Method,” *AIAA Journal*, Vol. 51, No. 7, 2013, pp. 1775–1779. <https://doi.org/10.2514/1.J052136>.
- [18] Beale, J. T., “A Convergent 3-D Vortex Method with Grid-Free Stretching,” *Mathematics of Computation*, Vol. 46, No. 174, 1986, pp. 401–424. <https://doi.org/10.2307/2007984>.
- [19] Williamson, J. H., “Low-Storage Runge-Kutta Schemes,” *Journal of Computational Physics*, Vol. 35, No. 1, 1980, pp. 48–56. [https://doi.org/10.1016/0021-9991\(80\)90033-9](https://doi.org/10.1016/0021-9991(80)90033-9).
- [20] Kolmogorov, A. N., “The Local Structure of Turbulence in Incompressible Viscous Fluid for Very Large Reynolds Numbers,” *Proceedings of the Royal Society A*, Vol. 434, No. 1890, 1991, pp. 9–13. <https://doi.org/10.1098/rspa.1991.0075>.
- [21] Vreman, A. W., “An Eddy-Viscosity Subgrid-Scale Model for Turbulent Shear Flow: Algebraic Theory and Applications,” *Physics of Fluids*, Vol. 16, No. 10, 2004, pp. 3670–3681. <https://doi.org/10.1063/1.1785131>.
- [22] Caradonna, F. X., and Tung, C., “Experimental and Analytical Studies of a Model Helicopter Rotor in Hover,” *NASA TM-81232*, 1981.
- [23] Cross, J. L., and Watts, M. E., “Tip Aerodynamics and Acoustic Test - A Report and Data Survey,” *NASA RP-1179*, 1988.
- [24] Sweet, G. E., “Hovering Measurements for Twin-Rotor Configurations With and Without Overlap,” *NASA TN-D-534*, 1960.
- [25] Fu, J., Yuan, Y., and Vigeveno, L., “Numerical Investigations of the Vortex Feature-Based Vorticity Confinement Models for the Assessment in Three-Dimensional Vortex-Dominated Flows,” *Meccanica*, Vol. 57, 2022, pp. 1657–1676. <https://doi.org/10.1007/s11012-022-01525-5>.
- [26] Lavoie, P., Bourgault-Côté, S., and Laurendeau, E., “Numerical algorithms for infinite swept wing ice accretion,” *Computers & Fluids*, Vol. 161, 2018, pp. 189–198. <https://doi.org/10.1016/j.compfluid.2017.11.015>.